Frontiers of Physics
https://doi.org/10.1007/s11467-020-1021-1

Front. Phys.
16(3), 33501 (2021)

RESEARCH ARTICLE

The unique carrier mobility of Janus MoSSe/GaN heterostructures

Wen-Jin Yin[1], Xiao-Long Zeng[1], Bo Wen[2], Qing-Xia Ge[1], Ying Xu[1],
Gilberto Teobaldi[3,4,5], Li-Min Liu[2,†]

[1] *School of Physics and Electronic Science, Hunan University of Science and Technology,*
Xiangtan 411201, China
[2] *School of Physics, Beihang University, Beijing 100083, China*
[3] *Scientific Computing Department, STFC UKRI, Rutherford Appleton Laboratory, Harwell Campus,*
OX11 0QX Didcot, United Kingdom
[4] *Stephenson Institute for Renewable Energy, Department of Chemistry, University of Liverpool,*
L69 3BX Liverpool, United Kingdom
[5] *School of Chemistry, University of Southampton, Highfield, SO17 1BJ Southampton, United Kingdom*
Corresponding author. E-mail: † *liminliu@buaa.edu.cn*

Received July 11, 2020; accepted September 2, 2020

Heterostructure is an effective approach in modulating the physical and chemical behavior of materials. Here, the first-principles calculations were carried out to explore the structural, electronic, and carrier mobility properties of Janus MoSSe/GaN heterostructures. This heterostructure exhibits a superior high carrier mobility of 281.28 $\mathrm{cm^2 \cdot V^{-1} \cdot s^{-1}}$ for electron carrier and 3951.2 $\mathrm{cm^2 \cdot V^{-1} \cdot s^{-1}}$ for hole carrier. Particularly, the magnitude of the carrier mobility can be further tuned by Janus structure and stacking modes of the heterostructure. It is revealed that the equivalent mass and elastic moduli strongly affect the carrier mobility of the heterostructure, while the deformation potential contributes to the different carrier mobility for electron and hole of the heterostructure. These results suggest that the Janus MoSSe/GaN heterostructures have many potential applications for the unique carrier mobility.

Keywords Janus heterostructure, carrier mobility, first-principles calculation

1 Introduction

The increasing development of technology triggers the revolution of electronic device or vehicle toward microminiaturization and multifunctional [1–3]. It is well known that size and intrinsic properties of a material are the two crucial factors. That means it should be in nanocrystalline, as well as own with desirable band gap and carrier mobility. The successful exfoliation of graphene shines the light on the potential of low dimensional material production. Meanwhile, it shows that graphene exhibits half-integer quantum hall effect, high migration rate, and mass less carrier transport properties [4]; however, the absence of band gap in pristine sheet leads to an extremely low on/off ratio, which severely limits its further application in nanoscale electronic device [4–6]. Thus, it has aroused extensive attention to modulate the electronic structure.

Structure tailoring is a common method to control the electronic property, such as forming armchair or zigzag edge nanoribbons. Although a small band gap can be opened, the carrier mobility would be dramatically reduced due to the missing of Dirac cone and scattering effect in the nanoribbons [7, 8]. For example, sub-10 nm nanoribbon field effect transistors showed that the carrier mobility was dropped to less than 200 $\mathrm{cm^2 \cdot V^{-1} \cdot s^{-1}}$ with diminishing width when the enough band gap opened [9]. On the other hand, introducing defect, doping, or surface modification can also regulate the electronic property of a material. But it is totally unavoidable to bring foreign atom into the system, where it will often serve as an electron or hole carrier trap site.

Apart from above approaches, searching for graphene analogue is fascinating, and shows strong vitality [10–12]. Transition metal dichalcogenides (TMDs) have received great interests. Through varying the collocation of chalcogenide S, Se, and Te atoms and transition metal Mo, W, Nb and V atoms, plenty of TMDs structures with tunable band gaps can be obtained [13, 14]. Single layer MoS_2, as a typical member of TMDs family, is a semiconductor with a band gap of about 1.9 eV [15], and it has been regarded as a promising candidate for field effect transistor with an on/off ratio exceeding 10^8 [16]. However, the previous result clearly showed that carrier mobility of a suspended MoS_2 sheet is found to be in the range of 0.5–3 $\mathrm{cm^2 \cdot V^{-1} \cdot s^{-1}}$, thus this small mobility will cause low ef-

---

*Special Topic: Heterojunction and Its Applications (Ed Chenghua Sun). This article can be also found at http://journal.hep.com.cn/fop/EN/10.1007/s11467-020-1021-1.

© Higher Education Press 2021

ficiency for the electronic devices [17–19]. Interestingly, Guo *et al.* found sorts of new metal oxides or sulfurs owing ultrahigh carrier mobility, together with superior oxidation resistance [20, 21]. Further work showed that through removing absorbates or depositing atop a high-dielectric layer, extrinsic scatters can be partially suppressed, and the value of carrier mobility can be increased to 200 $\mathrm{cm^2 \cdot V^{-1} \cdot s^{-1}}$ [22–25]. In addition, the magnitude of carrier mobility can also be remained in its armchair nanoribbons [26].

Recently, Lu *et al.* designed out a new kind of Janus TMDs MoSSe [27], which is obtained through breaking the out-of-plane structural symmetry of $\mathrm{MoS_2}$ [28, 29]. Superior to the $\mathrm{MoS_2}$, the Janus TMDs reported that an intrinsic dipole as well as large piezoelectricity could exist in the vertical direction of the Janus sheet [30–33]. Furthermore, theoretical result showed that the carrier mobility of single layer is about 157 $\mathrm{cm^2 \cdot V^{-1} \cdot s^{-1}}$ for hole carrier and 74 $\mathrm{cm^2 \cdot V^{-1} \cdot s^{-1}}$ for electron carrier. The carrier mobility can be further adjusted by varying the thickness like forming double or triple layers as homo heterostructure with the electron carrier at 1194 $\mathrm{cm^2 \cdot V^{-1} \cdot s^{-1}}$ and hole carrier at 5 894 $\mathrm{cm^2 \cdot V^{-1} \cdot s^{-1}}$ predicted by theoretical calculations [30]. Inspired by this, it is interesting to know the effect of heterostructure [34]. Because heterostructure cannot only preserve the property of its individual component, but also introduce advanced functional [35–37]. For example, the heterostructure of the different semiconductors could exhibit unusual band gap [38, 39]. What's more, intrinsic electric filed may generally exist in the heterostructure, and it would help to separate the carriers [40–42]. Meanwhile, Schottky barrier in the heterostructure [43] can also effectively reduce the recombination of electron-hole pairs and improve the life time of the carriers [44]. The formation of heterostructure requires the two components, owing some familiar behaviors. Luckily, the recent advancements in 2D group III–V compounds with simple wurtzite or zinc-blende structures like nitride GaN brings hope to further improve the single layer TMDs. The electronic band gap of single layer GaN can vary from 1.9 eV to 3.0 eV for different configurations [45]. The lattice parameters of GaN are quite similar to single layer TMDs [46]. And it has been reported that the formation of heterostructure with internal polarization can effectively reduce the band gap [47]. Thus, it is interesting to know the carrier behavior of the heterostructure between single layer Janus TMDs and nitride GaN.

In this work, we aim to unveil the structural and electronic properties of the Janus MoSSe/GaN heterostructure by the first-principles calculations. The outline of the paper can be organized as the following: Firstly, we systematically study the stabilities of the MoSSe/GaN heterostructures. Then, we examine the carrier mobility and the electronic behavior of the heterostructures. At last, the crucial factors on determining carrier mobility behavior will be discussed.

2 Computational method

All simulations were carried out at Density Functional Theory (DFT) level as implemented in the Vienna ab initio simulation program package (VASP) [48, 49], with the Perdew–Burke–Ernzerhof (PBE) exchange-correlation functional under the generalized gradient approximation (GGA) [50, 51]. The projector augmented wave (PAW) method was used to represent the electronic density at the atomic cores. The plane-wave energy cutoff was 500 eV and the converged energy is less than 1 meV per atom, checked to be sufficiently accurate against calculations with higher cutoffs. The convergence criterion for the self-consistency procedure was 10^{-6} eV. We used a 15×15×1 Monkhorst–Pack k-point grid in the Brillouin zone, with one k-point along the direction perpendicular to the 2D plane of the heterostructures. To avoid interactions between replicated images, a vacuum buffer of 20 Å was used. All the atomic positions in the systems were fully relaxed until the residual force were less than 0.001 eV/ Å on each atom. Van der Waals (vdW) interactions were treated at the DFT-D3 level [52].

The relative stability of the different heterostructure studied can be estimated by means of their formation energy, E_f, calculated as

$$E_f = E_{\mathrm{MoSSe/GaN}} - E_{\mathrm{MoSSe}} - E_{\mathrm{GaN}}. \tag{1}$$

$E_{\mathrm{MoSSe/GaN}}, E_{\mathrm{MoSSe}}$, and E_{GaN} are the total energy of the MoSSe/GaN heterostructure, and of the single-layer components (MoSSe and GaN) optimized in isolation at the same box, respectively. For the systems studied, the sign of E_f is negative in general as the systems pack via vdW interactions that are only attractive for a negligible interfacial relaxation. Thus, the more negative E_f, the larger the energetic favorability of the heterostructure.

The carrier mobility of the two-dimensional heterostructures can be calculated by the phonon-limited formula written as [53, 54]

$$\mu = \left(\mathrm{e}\hbar^3 C_{2D}\right) / \left[k_b T m^* m_d \left(E_i\right)^2\right]. \tag{2}$$

m^* is the effective mass (m_e^* for electron and m_d^* for the hole), where m_x and m_y refer to the effective mass along the x and y direction. $m_d^{e/h}$ is the equivalent mass defined as $m_d = \sqrt{m_x m_y}$ (m_d^e for electron and m_d^h for the hole). $E_i (i = e$ for the electron, $i = h$ for the hole) is the deformation potential, calculated as $E_i = \Delta E_i / (\Delta L_i / L_i)$. E_i can be obtained from the band-energy level change (ΔE_i) induced by a lattice compression or expansion of step $\Delta L_i / L_i = 0.005$ in the transport direction, where the reference energy level is set to the vacuum energy level. Based on this convention, the deformation potentials of one hole in the valence band maximum (VBM) and one electron in the conduction band minimum (CBM) are labelled as E_h and E_e, respectively. The elastic moduli of the longitudinal acoustic

C_{2D} in the propagation direction can be calculated as $C_{2D} = 2(E - E_0)/[S_0(\Delta L_i/L_i)^2]$, where E and E_0 are the total energy of the compressed/expanded and equilibrium geometries, respectively. S_0 is the area of two-dimensional material at the equilibrium geometry.

3 Results and discussion

The Janus MoSSe system has a honeycomb hexagonal lattice with three atomic layers as shown in Fig. 1(a). The optimized in plane lattice constant is $a = b = 3.215$ Å, with Mo-S and Mo-Se bond lengths of 2.41 Å and 2.53 Å, respectively. Similar to Janus MoSSe, single layer Nitride GaN has also a hexagonal symmetry, as shown in Fig. 1(b). Notably, the lattice constant of GaN is $a = b = 3.250$ Å, only 0.035 Å larger than that of MoSSe. Thus, a rather small ratio of lattice mismatch at about ~1.08% can be achieved, when MoSSe and GaN form a heterostructure. In Table 1, there includes other two single layer TMDs as MoS_2 and $MoSe_2$ with basic structure parameters, since they will be applied to form heterostructure in the context later.

These results indicate that MoSSe and GaN can form vertical vdW heterostructures (MoSSe/GaN in the following) with minimal in-plane strain. Due to the different faces of MoSSe, two arrangements are possible for such heterostructures, which we refer to as SMoSe/GaN and SeMoS/GaN. In addition, for each arrangement the individual layers can be stacked according to either an AA or AB staking pattern, see Figs. 1(c, d) and (e)–(h). For the AA-stacked SeMoS/GaN, the S atom can sit above the Ga [denoted as AA-[S-Ga] Fig. 1(c)] or the N atom [denoted as AA-[S-N] in Fig. 1(d)]. More combinations become possible for AB-stacking. For the Mo atom of SMoSe/GaN sitting above the hollow-site of the GaN hexagonal lattice, there are two kinds of possible AB-stacking depending on whether the Se atom sits above a Ga or N atom of the underlying GaN lattice. These structures are indicated as AB-[Se-Ga] or AB-[Se-N] as seen in Fig. 1(e) or (f). Conversely, for the Se atom of SMoSe/GaN sitting above the hollow-site of the GaN hexagonal lattice, two different AB-stacking are possible depending on whether the Mo atom sits on top of a Ga [AB-[Mo-Ga] in Fig. 1(g)] or N [AB-[Mo-N] in Fig. 1(h)] atom . In the following, the same labelling scheme is used also for the SeMoS/GaN heterostructure with S, not Se, atoms facing the underlying Ga/N layer.

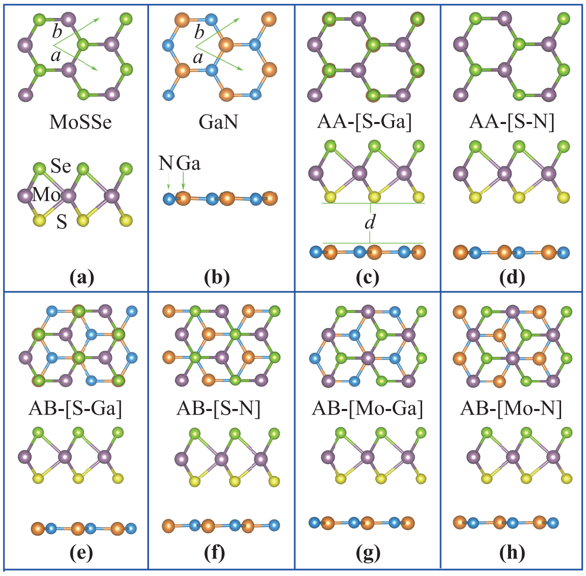

Fig. 1 The atomic structure of single layer MoSSe **(a)**, GaN **(b)**, and their AA **(c–d)** and AB stacked **(e–h)** heterostructures in type of SeMoS/GaN. The top and side views are in the upper and lower panels, respectively. The primitive cell is marked by the green arrows. The Mo, S, Se, Ga, and N atoms are shown as light violet, yellow, light green, orange, and gray spheres, respectively. The letter "d" denotes the interlayer distance between the top and bottom layer.

Table 1 The basic structural parameters for the selected single layer TMDs and GaN. The lattice mismatch needed to form the heterostructure and the magnitude of band gap (E_g) are also shown. I and D indicate direct and indirect band gap (E_g), respectively.

System	Lattice $a = b$ (Å)	Length (Å)		Angle (°)		Ratio of mismatch (%)	E_g (eV)
		Ga-N		∠GaNGa			
		Mo-S	Mo-Se	∠MoSMo	∠MoSeMo		
GaN	**3.250**	**1.87**		**120**		**0**	**1.98 (I)**
MoSSe	**3.215**	**2.41**	**2.53**	**83.73**	**79.09**	**1.08**	**1.67 (D)**
MoS_2	3.152	2.403		81.97		3.02	1.78 (D)
$MoSe_2$	3.287		2.53		80.86	1.14	1.54 (D)

Table 2 reports the calculated formation energy, lattice constant, interlayer distance, and band gap of the different MoSSe/GaN heterostructures studied. The simulations indicate that AB-[S-Ga] stacking results in the lowest E_f, of −0.266 eV in SeMoS/GaN, indicating this arrangement as the energetically favored. AA-[Se-Ga] stacking of the SMoSe/GaN heterostructure yields the second lowest E_f. Substitution of the upper MoSSe layer of the heterostructure with MoS_2 (SMoS) or $MoSe_2$ (SeMoSe) layers result in the AA-[S-Ga] (MoS_2/GaN) and AA-[Se-Ga] ($MoSe_2$/GaN) stacking being energetically favored with E_f of −0.212 eV and −0.265 eV, respectively. These results deviate from what previously calculated for heterostructures in graphene, for which AB-stacking is energetically favored [55]. Furthermore, we can also find that different stackings own different interlayer distance. This may be related to the possible atomic position and environment. Considering AA-[S-Ga] and AA-[S-N], the metal atom Ga is attractive to nonmetal S in AA-[S-Ga], while both nonmetal atom N and S in AA-[S-N] is repulsive to each other, leading to a larger interlayer distance of 3.5 Å

Table 2 The calculated formation energy (E_f), interlayer distance (d), and band gap (E_g) for the considered MoSSe/GaN heterostructures in different (AA or AB) stacking. I and D in brackets denote indirect and direct band gap, respectively.

Mode	Stacking	Lattice (Å)	E_f (eV)	d (Å)	E_g (eV)
SeMoS/GaN	**AA-[S-Ga]**	**3.234**	**−0.260**	**2.970**	**0.80 (D)**
	AA-[S-N]	3.233	−0.166	3.497	1.20 (D)
	AB-[Mo-Ga]	3.236	−0.239	2.993	1.25 (D)
	AB-[Mo-N]	3.234	−0.230	3.053	1.15 (D)
	AB-[S-Ga]	**3.239**	**−0.266**	**2.943**	**0.89 (D)**
	AB-[S-N]	3.233	−0.163	3.523	1.19 (D)
SMoSe /GaN	**AA-[Se-Ga]**	**3.237**	**−0.255**	**3.107**	**1.45 (D)**
	AA-[Se-N]	3.233	−0.227	3.22	1.52 (D)
	AB-[Ga-Mo]	3.234	−0.236	3.226	1.63 (D)
	AB-[Ga-N]	3.237	−0.230	3.053	1.15 (D)
	AB-[Se-Ga]	**3.238**	**−0.242**	**3.154**	**1.38 (D)**
	AB-[Se-N]	3.237	−0.167	3.592	1.62 (D)
SMoS /GaN	**AA-[S-Ga]**	**3.210**	**−0.212**	**2.988**	**0.77 (D)**
	AA-[S-N]	3.207	−0.121	3.036	1.13 (D)
SMoS /GaN	AB-[Mo-Ga]	3.208	−0.19	3.036	1.22 (D)
	AB-[Mo-N]	3.206	−0.184	3.103	1.13 (D)
	AB-[S-Ga]	**3.212**	**−0.209**	**2.967**	**0.84 (D)**
	AB-[S-N]	3.206	−0.118	3.526	1.12 (D)
SeMoSe /GaN	**AA-[Se-Ga]**	**3.265**	**−0.265**	**3.106**	**1.47 (D)**
	AA-[Se-N]	3.261	−0.172	3.573	1.56 (D)
SeMoSe /GaN	AB-[Mo-Ga]	3.263	−0.237	3.119	1.53 (D)
	AB-[Mo-N]	3.261	−0.241	3.169	1.59 (D)
	AB-[Se-Ga]	**3.266**	**−0.255**	**3.105**	**1.41 (D)**
	AB-[Se-N]	3.261	−0.170	3.609	1.54 (I)

in AA-[S-N]. The results in Table 2 indicates also that E_f for the AB-[S/Se-Ga] stacking in general is comparable (to within 0.013 eV) to the AA-[S/Se-Ga] one, suggesting these patterns to be energetically competitive and potentially accessible by experiments.

The lower formation energy is related to the different electron structure and interlayer distance of the heterostructure. As for SMoS/GaN, S atoms for AA-[S-Ga] in negative valence attracts the Ga atoms in positive valence with lower interlayer distance, resulting in stabilization of the heterostructure. Whereas the S atoms repels the N atoms in AA-[S-N] or other AB-stacking configurations and hence destabilizes the structures. Further, owing to the stronger oxidation of S atom than that of Se atom, the AA-[S-Ga] in SeMoS/GaN is about −0.01 eV lower than AA-[Se-Ga] in SMoSe/GaN. Except for the formation energy, the thermal stability of these heterostructures are also checked by first-principles molecular dynamics (FPMD). Here, we choose MoSSe/GaN heterostructure as a typical example. It is interesting to find that the structure remains unbroken for 2 ps FPMD at 300 K as shown in Fig. S1, suggesting the structure is thermal stable. Therefore, the results show that AB-[S-Ga] is more stable in SeMoS/GaN, while AA-[S/Se-Ga] is always more stable than other stackings for other heterostructures.

Besides the structural stability and formation energy, we analyzed also the electronic properties of the heterostructures studies. The corresponding results in Table 2 show that all the heterostructures studied are semiconductors regardless of the stacking type and relative atomic positions. The calculated band gap varies from 0.767 eV (SMoS/GaN, AA-[S-Ga]) to 1.631 eV (SMoSe/GaN, AB-[Ga-Mo]), which is located in the near visible-infrared region. Given the known underestimation errors the used PBE-GGA functional in calculating bandgap, these results suggest that visible light absorption for these systems may be possible. As also shown in Table 2, we find most of the heterostructures studied to have a direct band gap, in contrast with the indirect band gap for pristine GaN. Therefore, the simulations suggest that direct tuning of the electronic properties and, inevitably, light absorption of the heterostructures can be achieved by controlling the stacking geometry.

To further analyze the electronic properties of the lowest E_f heterostructures, we show their calculated band structures in Fig. 2. For all the systems, both the VBM and CBM are located at the K point, suggesting that all these heterostructures are direct semiconductors. By changing

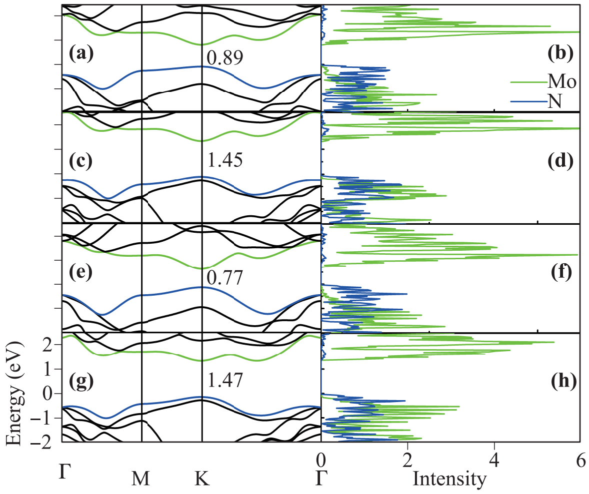

Fig. 2 The calculated electron band structure and atom-projected density of states (PDOS) for the energy favored stacking of the MoSSe/GaN, MoS_2/GaN and $MoSe_2$/GaN heterostructure. **(a, b)** AB-[S-Ga] stacked SeMoS/GaN, **(c, d)** AA-[Se-Ga] stacked SMoSe/GaN, **(d, e)** AA-[S-Ga] stacked MoS_2/GaN, and **(e, f)** AA-[Se-Ga] stacked $MoSe_2$/GaN. The lowest and highest energy bands in the CB and VB are shown in green and blue, respectively. The Mo and N resolved PDOS are shown in green and blue, respectively.

the position of the S and Se atoms with respect to the underlying GaN layer, the band gap can vary from 0.77 to 1.47 eV. In order to check the accuracy of PBE result, HSE hybrid functional was also considered. Here, we considered AB-[S-Ga] and AA-[S-Ga] of MoSSe/GaN as typical examples, and the corresponding band structures are shown in supporting information Fig. S2. It can be found that the band gaps are about 0.6 eV larger relative to the ones with PBE, but the tendency of the calculated band gaps with HSE is similar to the one with PBE.

To investigate the atomic contributions to VB and CB, Fig. 2 reports also the calculated electron, atom-projected density of states (PDOS). For clarity, only the main contributions to the VBM and CBM are provided. The results indicate that, for all the systems, the main contribution to the VBM stem from the N_{2p} orbitals (blue line) of GaN. Conversely, the main contributions to the CBM are due to the Mo_{3d} orbitals (green line) of MoSSe, MoS_2 and $MoSe_2$. Therefore, the CBM and VBM are distributed on different side of the heterostructure. This result can be straightforwardly visualized by the band-decomposed charge densities for the VBM and CBM, shown for SMoSe/GaN as model system in Fig. 3. Evidently, whereas the CBM charge density for AA-[Se-Ga] is mostly localized on the Mo atoms of the SMoSe layer, the VBM charge density is largest on the N atoms for the GaN layer. This intriguing property suggests that there is an intrinsic electronic field in the SMoSe/GaN heterostructure, which should be highly beneficial to separate photoinduced carriers.

The calculated dependence of the heterostructures electronic properties on the stacking geometry prompts for investigation of its role for carrier mobility too. We start by benchmarking the accuracy of our approach to electron effective mass and mobility for single layer MoS_2. We calculate an effective mass and carrier mobility of the electron in the CBM along X-K of 0.50 m_0 and 145.5 $\mathrm{cm^2{\cdot}V^{-1}{\cdot}s^{-1}}$, close to previously experimental result of 0.49 m_0 and 200 $\mathrm{cm^2{\cdot}V^{-1}{\cdot}s^{-1}}$ [19]. Literally, the calculated result is agree to the previous work, suggesting it is relatively reliable.

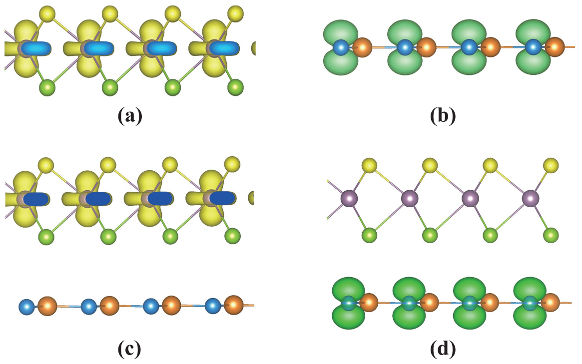

Fig. 3 **(a, b)** Side views of the density-distribution of the CBM in SMoSe (a) and of the VBM in GaN (b). **(c, d)** The side view of density-distribution of the the CBM and the VBM for the MoSSe bilayer. The isovalue for the contour plot is 0.01 e $\mathrm{bohr^{-3}}$.

Table 3 reports the calculated carriers m^*, m_d, E_i, C_{2D}, and μ for MoSSe/GaN, as well as MoS_2/GaN and $MoSe_2$/GaN in different stacking, together with results for single layer TMDs and GaN for comparison. For this analysis, we focus on the heterostructures with the lowest and second lowest E_f. Starting with MoSSe/GaN, the CBM of μ_e AB-[S-Ga] stacked SeMoS/GaN along the X-K path is about 263.28 $\mathrm{cm^2{\cdot}V^{-1}{\cdot}s^{-1}}$, which is nearly three times larger than for single layer MoSSe (97.83 $\mathrm{cm^2{\cdot}V^{-1}{\cdot}s^{-1}}$). Conversely, the VBM μ_h along the X-K path is about 3480.43 $\mathrm{cm^2{\cdot}V^{-1}{\cdot}s^{-1}}$, slightly smaller than for single layer GaN (3785.03 $\mathrm{cm^2{\cdot}V^{-1}{\cdot}s^{-1}}$). Qualitatively different results are computed for the other arrangements of the SMoSe/GaN heterostructure. The calculated μ_e and μ_h of AA-[Se-Ga] are increased to 281.28 and 3951.21 $\mathrm{cm^2{\cdot}V^{-1}{\cdot}s^{-1}}$, respectively. These values are larger than for the isolated MoSSe and GaN layers. Therefore, the simulations indicate that the carrier mobility of MoSSe/GaN heterostructures can be substantially, up to nearly three times, larger than for the individual components.

Analysis of the carrier mobility can be extended by considering the role of S or Se exposure to GaN for calculated results. As the Se atom in MoSSe is substituted by S to form the MoS_2/GaN heterostructure, the μ_e of AA-[S-Ga] decreases to 143.62 $\mathrm{cm^2{\cdot}V^{-1}{\cdot}s^{-1}}$. Also, the μ_h of AA-[S-Ga] stacked MoS_2/GaN decreases slightly (by 40.3 $\mathrm{cm^2{\cdot}V^{-1}{\cdot}s^{-1}}$) relative to the AA-[Se-GaN] stacking of MoSSe/GaN. In turn, as the S atom of MoSSe is changed into a Se atom to form $MoSe_2$/GaN heterostructure, the μ_e becomes 258.25 $\mathrm{cm^2{\cdot}V^{-1}{\cdot}s^{-1}}$ similar to the value for SMoSe/GaN. In contrast, the μ_h is strongly decreased by 3000 $\mathrm{cm^2{\cdot}V^{-1}{\cdot}s^{-1}}$. Thus, depending on the heterostructure composition, the μ_e can be tuned from 143.62 $\mathrm{cm^2{\cdot}V^{-1}{\cdot}s^{-1}}$ to 281.28 $\mathrm{cm^2{\cdot}V^{-1}{\cdot}s^{-1}}$ in the CBM, and the μ_h from 791.34 $\mathrm{cm^2{\cdot}V^{-1}{\cdot}s^{-1}}$ to 3951.21 $\mathrm{cm^2{\cdot}V^{-1}{\cdot}s^{-1}}$ in the VBM.

The simulations reveal an important role also of the heterostructure stacking for its carrier mobility. For instance, the μ_e and μ_h of AA-[S-Ga] stacked SeMoS/GaN are about 13.82 and 1002 $\mathrm{cm^2{\cdot}V^{-1}{\cdot}s^{-1}}$ smaller than for the analogous AB-[S-Ga] stacked system. This trend is different from what shown by the other systems studied, for which AA stacking is found to increase carrier mobility. Taking SMoSe/GaN as an example, the μ_e and μ_h of AA-[Se-Ga] is increased by 8.38 and 259.06 $\mathrm{cm^2{\cdot}V^{-1}{\cdot}s^{-1}}$ compared to AB-[Se-Ga]. Thus, we find that, depending on the AB or AA stacking, carrier mobility can be tuned by 19–123 $\mathrm{cm^2{\cdot}V^{-1}{\cdot}s^{-1}}$ for electrons, and by 259–1002 $\mathrm{cm^2{\cdot}V^{-1}{\cdot}s^{-1}}$ for holes. Comparing these results with the substantially larger compositional changes analyzed above, we are to conclude that carrier mobility in the con-

Table 3 The calculated carrier mobility at 300 K for the (lowest and second lowest E_f) MoSSe/GaN, MoS_2/GaN, and $MoSe_2$/GaN heterostructures. The results for single layer Janus MoSSe, MoS_2, $MoSe_2$, and GaN are also provided for comparison. m_e^*/m_h^*: the effective electron/hole mass, m_d^e/m_d^h: the effective equivalent electron/hole mass, E_e/E_h: the electron/hole deformation potential, C_{2D}: the elastic moduli, and μ_e/μ_h the electron/hole carrier mobility at CBM and VBM. It should be mentioned that only lowest E_f and second lowest E_f cases are considered.

System		$m_e{}^*$	m_d^e	m_h^*	m_d^h	E_e	E_h	C_{2D}	μ_e	μ_h
GaN		0.22	0.72	1.27	0.89	10.6	0.84	140.2	171.10	3785.03
MoS_2		0.50	0.62	0.60	1.57	8.22	2.30	141.15	145.50	605.44
MoSSe		0.56	0.62	0.68	2.61	8.46	2.83	115.39	97.83	173.65
$MoSe_2$		0.53	0.5	0.64	2.42	6.94	2.16	204.12	263.15	600.77
SeMoS/GaN	AA-[S-Ga]	0.53	0.66	1.49	1.06	8.0	1.20	264.10	249.46	2478.36
	AB-[S-Ga]	**0.55**	**0.65**	**1.80**	**1.26**	**7.66**	**0.84**	**258.98**	**263.28**	**3480.43**
SMoSe/GaN	**AA-[Se-Ga]**	**0.54**	**0.7**	**1.23**	**1.45**	**7.47**	**0.91**	**275.5**	**281.28**	**3951.21**
	AB-[Se-Ga]	0.52	0.70	1.82	0.84	7.62	1.00	266.86	272.90	3692.15
MoS_2/GaN	**AA-[S-Ga]**	**0.44**	**1.47**	**1.27**	**1.17**	**8.05**	**1.02**	**273.87**	**143.62**	**3910.91**
	AB-[S-Ga]	0.44	1.53	1.49	1.07	6.24	2.83	277.79	266.93	3050.20
$MoSe_2$/GaN	**AA-[Se-Ga]**	**0.73**	**0.69**	**1.39**	**1.14**	**6.66**	**2.16**	**271.91**	**258.25**	**791.34**
	AB-[Se-Ga]	0.61	0.68	1.00	0.99	8.41	1.81	265.58	191.53	1739.03

sidered heterostructures are substantially more sensitive to the occurrence of S/GaN or Se/GaN interfaces rather than AA or AB stacking.

In order to identify the diverse carrier mobility in heterostructures studied, we systemically calculated carriers effective and equivalent mass, deformation potential, and elastic moduli for the heterostructures as well as their individual component as shown in Table 3. Identification of the crucial factor(s) behind the carrier mobility is essential for definition of synthetic strategies to enhance it. Taking AA-[Se-Ga] stacked SMoSe/GaN as case study, the μ_e is about 2 times that of MoSSe, and the μ_h is close to isolated GaN layer. However, the ratio of m_e^*, m_d^e, E_e, and C_{2D} between AA-[Se-Ga] and MoSSe is about 0.98, 1.13, 0.88, and 2.4, while the ratio of m_h^*, m_d^h, E_h, and C_{2D} between AA-[Se-Ga] and GaN is about 0.97, 1.63, 1.08, and 1.96. According to Eq. (2) m^*, m_d, and E_i are inversely proportional, while the C_{2D} is linearly proportional to the μ. Thus, it can be deduced that the μ_e is strongly relative to the C_{2D}, whereas the μ_h is also related to m_d. The case for AA-[S-Ga] of MoS_2/GaN is a little different, where the is μ_e close to that of MoS_2, and the μ_h is a little larger than isolated GaN layer. The ratio of m_e^*, m_d^e, E_e, and C_{2D} between AA-[S-Ga] and MoS_2 is about 0.88, 2.37, 0.98, and 1.94, while the ratio of m_h^*, m_d^h, E_h, and C_{2D} between AA-[S-Ga] and GaN is about 1.00, 1.31, 1.21, and 1.94. So, it can be found that the μ_e is strongly affected by m_d^e, where as the μ_h is much sensitive to E_h. As a result, we can find that the carrier mobility is strongly affected by larger equivalent mass and elastic moduli, meanwhile, the hole carrier mobility is also related to deformation potential. As for the larger equivalent mass, it can clearly see from the extremely flat character of the CMB along the Γ-M path (Fig. 2). Considering elastic moduli, the larger elastic moduli in heterostructure should origin from the thicker thickness in heterostructure compared with those of its single component.

Then, it is interesting to know the reason why electron and hole behaves markedly differently. As for SMoSe/GaN, the electron mobility of AA-[Se-Ga] is 281.28 $cm^2 \cdot V^{-1} \cdot s^{-1}$, while the hole mobility is 3951.21 $cm^2 \cdot V^{-1} \cdot s^{-1}$ about 14 times larger than for the electron. The ratio of effective mass, equivalent mass, deformation potential, and elastic moduli between hole and electron are about 2.23, 2.1, 0.12, and 1.0. Accordingly, we are to infer that the deformation potential should be the dominant factor. The different deformation potential can be seen from the different bonding characteristic of valence band and conduction band. For the electron in CBM, the charge distribution is mainly localized in the x–y plane in Mo_{3d} orbitals [see Fig. 3(c)], which is larger than the distribution of VBM with the electron localized only at N_{2p} orbitals [see Fig. 3(d)]. As structural deformation occurs, it will generate stronger electrostatic interaction in CBM than that in VBM, corresponding to larger E_e than E_h. Therefore, smaller deformation potential contributes to larger μ_h for the heterostructure.

As discussed above, the electron and hole carrier mobility can also be influenced by stacking of the heterostructure. As for stacking effect, the result indicates that the carrier mobility of second lowest E_f structure is always smaller than for the lowest E_f stacking. This difference should origin from a slight larger equivalent mass and deformation potential of the distinct atoms.

4 Conclusion

In summary, the structural, electronic and carrier mobility properties of MoSSe/GaN heterostructures were systematically investigated by the first-principles calculations. It shows that Janus MoSSe/GaN heterostructure has a relatively high carrier mobility of 281.28 $\mathrm{cm^2 \cdot V^{-1} \cdot s^{-1}}$ for electron carrier and 3951.2 $\mathrm{cm^2 \cdot V^{-1} \cdot s^{-1}}$ for hole carrier. Except the intrinsic electric field of Janus MoSSe, the carrier mobility can be further regulated through the different stacking strategies and Janus atomic structure of MoSSe. The results further indicate that the superior carrier mobility of Janus MoSSe/GaN heterostructure are affected by the equivalent mass and elastic moduli. These results showed that the Janus MoSSe/GaN heterostructure has a potential to be used as electronic device for their carrier mobility.

Acknowledgements This work was supported by the Science Challenge Project (Grant No. TZ2018004), the National Natural Science Foundation of China (Grant Nos. 51572016, U1530401, 11747167, 11804090, 51472209, 11774298, U1401241, and 21503012), the Natural Science Foundation of Hunan Province, China (Grant Nos. 17C0626 and 2019JJ50148). This research was also supported by a Tianhe-2JK computing time award at the Beijing Computational Science Research Center (CSRC). L. M. L. and G. T. acknowledge also support by the Royal Society Newton Advanced Fellowship scheme (Grant No. NAF\R1\180242).

Supplementary information

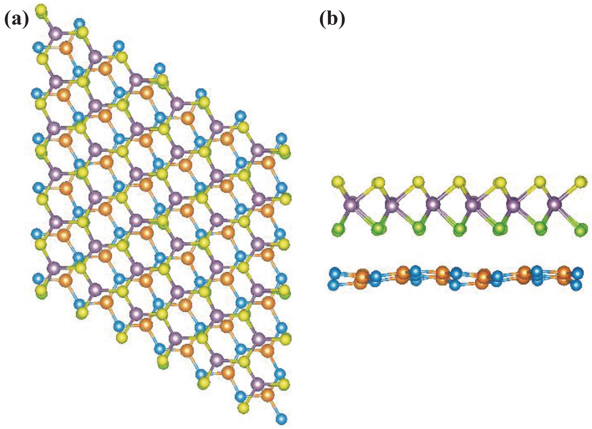

Fig. S1 The structure of the MoSSe/GaN after 2 ps simulation at 300 K. **(a)** The top view of the structure and **(b)** side view of the structure. The Mo, S, Se, Ga, and N atoms are shown as light violet, yellow, light green, orange, and gray spheres, respectively. The letter "d" denotes the interlayer distance between the top and bottom layer.

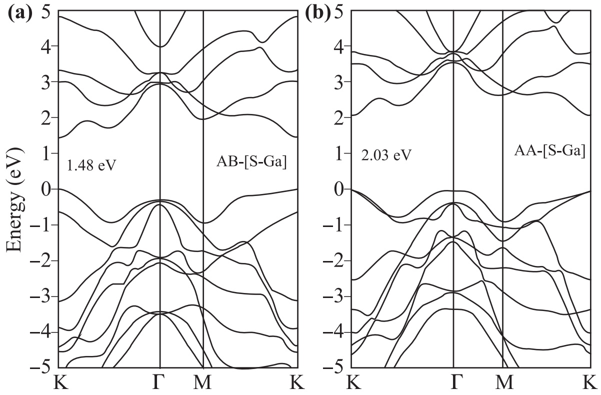

Fig. S2 The band structure of MoSSe/GaN heterostructure calculated by HSE hybrid functional. **(a)** AB-[S-Ga] stacked SeMoS/GaN, **(b)** AA-[S-Ga] stacked SMoSe/ GaN.

References

1. Y. Gao, T. Cao, F. Cellini, C. Berger, W. A. de Heer, E. Tosatti, E. Riedo, and A. Bongiorno, Ultrahard carbon film from epitaxial two-layer graphene, *Nat. Nanotechnol.* 13(2), 133 (2018)
2. C. Tan, X. Cao, X. J. Wu, Q. He, J. Yang, X. Zhang, J. Chen, W. Zhao, S. Han, G. H. Nam, M. Sindoro, and H. Zhang, Recent advances in ultrathin two-dimensional nanomaterials, *Chem. Rev.* 117(9), 6225 (2017)
3. W. J. Yin, B. Wen, C. Zhou, A. Selloni, and L. M. Liu, Excess electrons in reduced rutile and anatase $\mathrm{TiO_2}$, *Surf. Sci. Rep.* 73(2), 58 (2018)
4. M. Wang, Y. Pang, D. Y. Liu, S. H. Zheng, and Q. L. Song, Tuning magnetism by strain and external electric field in zigzag Janus MoSSe nanoribbons, *Comput. Mater. Sci.* 146, 240 (2018)
5. A. K. Geim, Graphene: Status and prospects, *Science* 324(5934), 1530 (2009)
6. K. S. Novoselov, A. K. Geim, S. V. Morozov, D. Jiang, Y. Zhang, S. V. Dubonos, I. V. Grigorieva, and A. A. Firsov, Electric field effect in atomically thin carbon films, *Science* 306(5696), 666 (2004)
7. C. Lin, D. Shin, and A. A. Demkov, Localized states induced by an oxygen vacancy in rutile $\mathrm{TiO_2}$, *J. Appl. Phys.* 117(22), 225703 (2015)
8. Z. K. Han, Y. Z. Yang, B. Zhu, M. V. Ganduglia-Pirovano, and Y. Gao, Unraveling the oxygen vacancy structures at the reduced $\mathrm{CeO_2}$ (111) surface, *Phys. Rev. Mater.* 2(3), 035802 (2018)
9. T. Umebayashi, T. Yamaki, H. Itoh, and K. Asai, Analysis of electronic structures of 3d transition metal-doped $\mathrm{TiO_2}$ based on band calculations, *J. Phys. Chem. Solids* 63(10), 1909 (2002)
10. H. C. Yang, Y. Xie, J. Hou, A. K. Cheetham, V. Chen, and S. B. Darling, Janus membranes: Creating asymmetry for energy efficiency, *Adv. Mater.* 30(43), 1801495 (2018)

11. H. Zhang, Y.N. Zhang, H. Liu, and L.M. Liu, Novel heterostructures by stacking layered molybdenum disulfides and nitrides for solar energy conversion, *J. Mater. Chem. A* 2(37), 15389 (2014)
12. Y. Gong, H. Yuan, C. L. Wu, P. Tang, S. Z. Yang, A. Yang, G. Li, B. Liu, J. van de Groep, M. L. Brongersma, M. F. Chisholm, S. C. Zhang, W. Zhou, and Y. Cui, Spatially controlled doping of two-dimensional SnS_2 through intercalation for electronics, *Nat. Nanotechnol.* 13(4), 294 (2018)
13. M. Chhowalla, H. S. Shin, G. Eda, L. J. Li, K. P. Loh, and H. Zhang, The chemistry of two-dimensional layered transition metal dichalcogenide nanosheets, *Nat. Chem.* 5(4), 263 (2013)
14. C. Ataca, H. Şahin, and S. Ciraci, Stable, single-layer MX_2 transition-metal oxides and dichalcogenides in a honeycomb-like structure, *J. Phys. Chem. C* 116(16), 8983 (2012)
15. Q. Xiang, J. Yu, and M. Jaroniec, Synergetic effect of MoS_2 and graphene as cocatalysts for enhanced photocatalytic H_2 production activity of TiO_2 nanoparticles, *J. Am. Chem. Soc.* 134(15), 6575 (2012)
16. B. Radisavljevic and A. Kis, Mobility engineering and a metal–insulator transition in monolayer MoS_2, *Nat. Mater.* 12(9), 815 (2013)
17. W. S. Yun, S. W. Han, S. C. Hong, I. G. Kim, and J. D. Lee, Thickness and strain effects on electronic structures of transition metal dichalcogenides: 2H-MX_2 semiconductors (M = Mo, W; X = S, Se, Te), *Phys. Rev. B* 85(3), 033305 (2012)
18. S. Fathipour, N. Ma, W. S. Hwang, V. Protasenko, S. Vishwanath, H. G. Xing, H. Xu, D. Jena, J. Appenzeller, and A. Seabaugh, Exfoliated multilayer $MoTe_2$ field-effect transistors, *Appl. Phys. Lett.* 105(19), 192101 (2014)
19. B. Radisavljevic, A. Radenovic, J. Brivio, V. Giacometti, and A. Kis, Single-layer MoS_2 transistors, *Nat. Nanotech.* 6, 147 (2011)
20. Y. Guo, Q. Wu, Y. Li, N. Lu, K. Mao, Y. Bai, J. Zhao, J. Wang, and X. C. Zeng, Copper(I) sulfide: A two-dimensional semiconductor with superior oxidation resistance and high carrier mobility, *Nanoscale Horizons* 4(1), 223 (2019)
21. Y. Guo, L. Ma, K. Mao, M. Ju, Y. Bai, J. Zhao, and X. C. Zeng, Eighteen functional monolayer metal oxides: wide bandgap semiconductors with superior oxidation resistance and ultrahigh carrier mobility, *Nanoscale Horizons* 4(3), 592 (2019)
22. G. Mattioli, F. Filippone, P. Alippi, and A. Amore Bonapasta, *Ab initio* study of the electronic states induced by oxygen vacancies in rutile and anatase, *Phys. Rev. B* 78, 241201(R) (2008)
23. S. Najmaei, Z. Liu, W. Zhou, X. Zou, G. Shi, S. Lei, B. I. Yakobson, J.C. Idrobo, P. M. Ajayan, and J. Lou, Vapour phase growth and grain boundary structure of molybdenum disulphide atomic layers, *Nat. Mater.* 12(8), 754 (2013)
24. X. Ma, X. Wu, H. Wang, and Y. Wang, A Janus MoSSe monolayer: A potential wide solar-spectrum water-splitting photocatalyst with a low carrier recombination rate, *J. Mater. Chem. A* 6(5), 2295 (2018)
25. R. Chaurasiya and A. Dixit, Defect engineered MoSSe Janus monolayer as a promising two dimensional material for NO_2 and NO gas sensing, *Appl. Surf. Sci.* 490, 204 (2019)
26. Y. Cai, G. Zhang, and Y. W. Zhang, Polarity-reversed robust carrier mobility in monolayer MoS_2 nanoribbons, *J. Am. Chem. Soc.* 136(17), 6269 (2014)
27. A. Y. Lu, H. Zhu, J. Xiao, C. P. Chuu, Y. Han, M. H. Chiu, C. C. Cheng, C. W. Yang, K. H. Wei, Y. Yang, Y. Wang, D. Sokaras, D. Nordlund, P. Yang, D. A. Muller, M.Y. Chou, X. Zhang, and L. J. Li, Janus monolayers of transition metal dichalcogenides, *Nat. Nanotechnol.* 12(8), 744 (2017)
28. J. Zhang, S. Jia, I. Kholmanov, L. Dong, D. Er, W. Chen, H. Guo, Z. Jin, V. B. Shenoy, L. Shi, and J. Lou, Janus monolayer transition-metal dichalcogenides, *ACS Nano* 11(8), 8192 (2017)
29. R. Peng, Y. Ma, S. Zhang, B. Huang, and Y. Dai, Valley polarization in janus single-layer MoSSe via magnetic doping, *J. Phys. Chem. Lett.* 9(13), 3612 (2018)
30. W. J. Yin, B. Wen, G. Z. Nie, X. L. Wei, and L. M. Liu, Tunable dipole and carrier mobility for a few layer Janus MoSSe structure, *J. Mater. Chem. C* 6(7), 1693 (2018)
31. H. C. Yang, J. Hou, V. Chen, and Z. K. Xu, Janus membranes: Exploring duality for advanced separation, *Angew. Chem. Int. Ed. Engl.* 55(43), 13398 (2016)
32. Y. Guo, S. Zhou, Y. Bai, and J. Zhao, Enhanced piezoelectric effect in Janus group-III chalcogenide monolayers, *Appl. Phys. Lett.* 110(16), 163102 (2017)
33. L. Dong, J. Lou, and V. B. Shenoy, Large in-plane and vertical piezoelectricity in Janus transition metal dichalchogenides, *ACS Nano* 11(8), 8242 (2017)
34. H. L. Wang, L. S. Zhang, Z. G. Chen, J. Q. Hu, S. J. Li, Z. H. Wang, J. S. Liu, and X. C. Wang, Semiconductor heterojunction photocatalysts: design, construction, and photocatalytic performances, *Chem. Soc. Rev.* 43(15), 5234 (2014)
35. Y. Ding, J. Shi, C. Xia, M. Zhang, J. Du, P. Huang, M. Wu, H. Wang, Y. Cen, and S. Pan, Enhancement of hole mobility in InSe monolayer via an InSe and black phosphorus heterostructure, *Nanoscale* 9(38), 14682 (2017)
36. F. B. Zheng, L. Zhang, J. Zhang, P. Wang, and C. W. Zhang, Germanene/GaGeTe heterostructure: A promising electric-field induced data storage device with high carrier mobility, *Phys. Chem. Chem. Phys.* 22(9), 5163 (2020)
37. Y. Yao, J. Cao, W. Yin, L. Yang, and X. Wei, A 2D ZnSe/BiOX vertical heterostructure as a promising photocatalyst for water splitting: A first-principles study, *J. Phys. D Appl. Phys.* 53(5), 055108 (2020)
38. W. Li, Z. Lin, and G. Yang, A 2D self-assembled MoS_2 /$ZnIn_2S_4$ heterostructure for efficient photocatalytic hydrogen evolution, *Nanoscale* 9(46), 18290 (2017)

39. X. Sun, H. Deng, W. Zhu, Z. Yu, C. Wu, and Y. Xie, Interface engineering in two-dimensional heterostructures: Towards an advanced catalyst for ullmann couplings, *Angew. Chem. Int. Ed. Engl.* 55(5), 1704 (2016)
40. Z. Wei, F. F. Liang, Y. F. Liu, W. J. Luo, J. Wang, W. Q. Yao, and Y. F. Zhu, Photoelectrocatalytic degradation of phenol-containing wastewater by TiO_2/g-C_3N_4hybrid heterostructure thin film, *Appl. Catal. B* 201, 600 (2017)
41. W. Yin, B. Wen, Q. Ge, D. Zou, Y. Xu, M. Liu, X. Wei, M. Chen, and X. Fan, Role of intrinsic dipole on photocatalytic water splitting for Janus MoSSe/nitrides heterostructure: A first-principles study, *Prog. Nat. Sci.: Mater. Inter.* 29, 335 (2019)
42. W. Yin, B. Wen, Q. Ge, X. Wei, G. Teobaldi, and L. Liu, Effect of crystal field on the formation and diffusion of oxygen vacancy at anatase (101) surface and sub-surface, *Prog. Nat. Sci.: Mater. Inter.* 30(1), 128 (2020)
43. M. L. Sun, J. P. Chou, Q. Q. Ren, Y. M. Zhao, J. Yu, and W. C. Tang, Tunable Schottky barrier in van der Waals heterostructures of graphene and g-GaN, *Appl. Phys. Lett.* 110(17), 173105 (2017)
44. L. Zhou, Y. Dai, J. Guo, R. Chen, Y. Xie, and W. Luo, Novel $Ag_3PO_4/LaCo_{1-x}Bi_xO_3$ composite photocatalyst with enhanced photocatalytic degradation of BPA under visible light, *Mater. Lett.* 213, 387 (2018)
45. Z. Y. Al Balushi, K. Wang, R. K. Ghosh, R. A. Vilá, S. M. Eichfeld, J. D. Caldwell, X. Qin, Y.C. Lin, P. A. DeSario, G. Stone, S. Subramanian, D. F. Paul, R. M. Wallace, S. Datta, J. M. Redwing, and J. A. Robinson, Two-dimensional gallium nitride realized via graphene encapsulation, *Nat. Mater.* 15(11), 1166 (2016)
46. Y. Zhao, H. Wang, H. Zhou, and T. Lin, Directional fluid transport in thin porous materials and its functional applications, *Small* 13(4), 1601070 (2017)
47. X. Li, Z. Li, and J. Yang, Proposed photosynthesis method for producing hydrogen from dissociated water molecules using incident near-infrared light, *Phys. Rev. Lett.* 112(1), 018301 (2014)
48. G. Kresse and J. Hafner, *Ab initio* molecular dynamics for liquid metals, *Phys. Rev. B* 47(1), 558 (1993)
49. G. Kresse and J. Furthmüller, Efficient iterative schemes for *ab initio* total-energy calculations using a plane-wave basis set., *Phys. Rev. B* 54(16), 11169 (1996)
50. J. P. Perdew, K. Burke, and M. Ernzerhof, Generalized gradient approximation made simple, *Phys. Rev. Lett.* 77(18), 3865 (1996)
51. J. P. Perdew, K. Burke, and M. Ernzerhof, Generalized gradient approximation made simple [*Phys. Rev. Lett.* 77, 3865 (1996)], *Phys. Rev. Lett.* 78(7), 1396 (1997)
52. S. Grimme, J. Antony, S. Ehrlich, and H. Krieg, A consistent and accurate *ab initio* parametrization of density functional dispersion correction (DFT-D) for the 94 elements H-Pu, *J. Chem. Phys.* 132, 154104 (2010)
53. X. B. Li, P. Guo, Y. N. Zhang, R. F. Peng, H. Zhang, and L. M. Liu, High carrier mobility of few-layer PbX (X = S, Se, Te), *J. Mater. Chem. C* 3(24), 6284 (2015)
54. S. Bruzzone and G. Fiori, *Ab-initio* simulations of deformation potentials and electron mobility in chemically modified graphene and two-dimensional hexagonal boronnitride, *Appl. Phys. Lett.* 99(22), 222108 (2011)
55. C. L. Lu, C. P. Chang, Y. C. Huang, R. B. Chen, and M. L. Lin, Influence of an electric field on the optical properties of few-layer graphene with *AB* stacking, *Phys. Rev. B* 73(14), 144427 (2006)